



Explanation of the patterns in Mie theory

M.J. Berg^a, C.M. Sorensen^{b,*}, A. Chakrabarti^b

^a US Army Research Laboratory, RDRL-CIE-S, 2800 Powder Mill Road, Adelphi, MD 20783-1197, USA

^b Kansas State University, Department of Physics, Manhattan, KS 66506-2601, USA

ARTICLE INFO

Article history:

Received 11 September 2009

Received in revised form

5 November 2009

Accepted 6 November 2009

Keywords:

Electromagnetic scattering

Light scattering

Mie theory

Guinier law

Porod law

Phase function

ABSTRACT

The far-field scattered light intensity, or the related phase function, for a spherical particle is known to display an overall power-law structure when formulated in terms of the scattering wave vector. Empirically determined patterns in the intensity relating to the particle size and refractive index are known. The cause of the patterns, however, has not been satisfactorily explained. This work applies an exact microphysical model to explain most of the patterns, and specifically, to reveal the physical cause of crossovers from one power-law to another. A unique aspect of this microphysical approach is phasor analysis, which provides a visually based way to examine the angle-dependent wavelet superposition involved in the model. A simple color coding scheme connects the phasors to the interior of the particle, and it is this connection that reveals the meaning of the crossovers.

© 2009 Elsevier Ltd. All rights reserved.

1. Introduction

In the far-field zone of a uniform spherical particle, the scattered light intensity provided by Mie theory is known to display an overall power-law structure [1,2]. This power-law structure is seen when the intensity distribution is formulated in terms of the scattering wave vector q , rather than in terms of the polar and azimuthal angles. Patterns appear in the power-law structure as the particle radius R and refractive index m are varied. An *empirically based* study of these patterns reveals simple relationships between R and the real part of m and characteristic features in the far-field angular scattered intensity distribution [1]. These empirical relationships make the patterns useful in situations where one desires a simple method to identify estimates for R and $\text{Re}\{m\}$ directly from the scattered intensity, or the related phase function. Moreover, the simplicity of the patterns allows one to

semi-quantitatively describe the form of the angular intensity for *any* spherical particle without recourse to sophisticated numerical calculation. Since their discovery, the patterns have received attention in both theoretical and experimental contexts [3–11]. Examples of laboratory measurements displaying the patterns can be found in [1,5,9,12].

In principle, the explanation for the occurrence and quantitative form of the power-law patterns is contained in the Mie solution. Unfortunately though, the mathematical complexity of the solution obscures a clear identification of their cause and physical significance. Consequently, simple models have been presented that explain the patterns using scaling arguments, Huygens' principle, and ray-tracing [1,8]. While these models can account for much of the patterns, certain inherent assumptions prevent them from being convincing and general explanations.

The purpose of this work is to apply an exact microphysical model to explain the origin of the patterns and the physical meaning of their various indicative features. The following will first present a short review of the q -space concept, the patterns, and the microphysical

* Corresponding author.

E-mail addresses: matt.berg@arl.army.mil (M.J. Berg), sor@phys.ksu.edu (C.M. Sorensen).

model. The model will then be applied to the problem of scattering by a single spherical particle in the weak and strong refraction regimes. These regimes are quantified by when the particle's phase shift parameter ρ , Eq. (4), is less than one and greater than one, respectively. A graphically based technique describing the scattering process, called phasor analysis, will be applied to both the $\rho < 1$ and $\rho > 1$ cases. Although a considerable amount of analysis will be required, the key points of this work will be to show that:

- The power-law form of the scattered intensity is related to the curvature of the particle's surface.
- Transitions between power-law regimes, called crossovers, are caused by the onset of destructive interference over specific regions within the particle.
- Characteristic length scales of the particle are associated with the crossovers.

All in all, this work will provide one with a conceptual interference-based understanding for the cause of the overall form of a spherical particle's far-field scattered intensity distribution.

2. Background: q -space and the patterns

Consider a spherical particle of volume V_{int} located at the origin \mathcal{O} of the coordinate system. For simplicity, the particle is assumed to reside in vacuum and have only real-valued refractive index m . Illuminating the particle is a linearly polarized electromagnetic plane wave traveling in the $\hat{\mathbf{n}}^{inc}$ direction. The electric field of this incident wave is given by

$$\mathbf{E}^{inc}(\mathbf{r}) = \mathbf{E}_0^{inc} \exp(ik\mathbf{r}\hat{\mathbf{n}}^{inc}), \quad (1)$$

where \mathbf{E}_0^{inc} is a constant vector describing the amplitude and polarization of the wave and k is the wavenumber given by $k = 2\pi/\lambda$ where λ is the vacuum wavelength. All field quantities in this work are assumed to be time-harmonic and described by the factor $\exp(-i\omega t)$, where $\omega = kc$, with c being the speed of light. This global time

factor will be suppressed for brevity. A detector is located at the observation point \mathbf{r} , which resides in the horizontal scattering plane. This plane is perpendicular to the polarization of the incident field. It will be convenient in the following to take $\mathbf{E}_0^{inc} = E_0^{inc}\hat{\mathbf{x}}$, where E_0^{inc} is a real-valued constant and $\hat{\mathbf{n}}^{inc} = \hat{\mathbf{z}}$. Then, the detector resides in the y - z plane through the origin, see Fig. 1. Also, the detector is assumed to remain at a fixed radial distance R_l from the particle, i.e., $\mathbf{r} = R_l\hat{\mathbf{r}}$, where the size of the constant R_l is such that \mathbf{r} resides in the particle's far-field zone following [13].

The power-law patterns appear when the far-field scattered intensity I is plotted log-log in terms of the scattering wave vector \mathbf{q} , rather than in terms of the polar scattering angle θ . This vector represents the difference in momentum between the incident plane wave and the far-field scattered wave in the $\hat{\mathbf{r}}$ direction, see Fig. 1 [22],

$$\mathbf{q} = k(\hat{\mathbf{n}}^{inc} - \hat{\mathbf{r}}). \quad (2)$$

The magnitude of \mathbf{q} depends on θ as

$$q(\theta) = 2k\sin\left(\frac{\theta}{2}\right), \quad (3)$$

and has the units of inverse length. Note that \mathbf{q} lies in the same scattering plane as \mathbf{r} . In the following, the dependence of q on θ will be tacitly assumed and suppressed for brevity.

The semi-log plot (a) in Fig. 2 shows the evolution of the normalized intensity for spherical particles with various size parameters kR . These curves are generated from Mie theory following [20] using a refractive index of $m = 1.05$. Plot (b) shows the same intensity curves, except plotted log-log as a function of the unitless quantity qR . One can see from (b) that all of the intensity curves are roughly bounded by linear envelopes, which given the log-log scale, indicates an overall power-law dependence of I on qR . In a sense, one can regard the envelopes as a coarse average of the more detailed ripple structure. In contrast, notice that the decay of the curves in (a) with angle does not clearly display a *specific* power-law form nor a transition from one power-law to another. The term

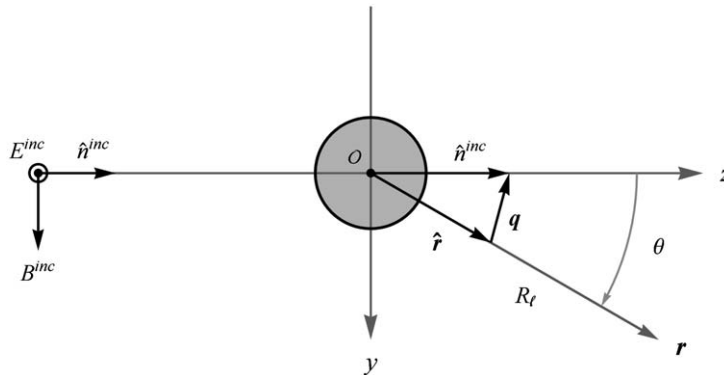


Fig. 1. Scattering arrangement consisting of a spherical particle illuminated by a linearly polarized plane wave. The observation point \mathbf{r} is confined to the y - z plane at a fixed radial distance R_l from the particle. The polarization of the incident wave is normal to y - z plane. Also indicated is the direction of the scattering wave vector \mathbf{q} , Eq. (2).

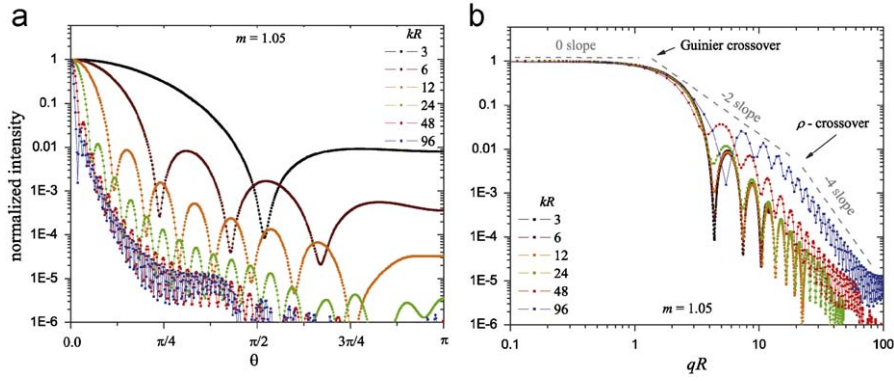


Fig. 2. Power-law structure of the normalized scattered intensity I for spherical particles with $m = 1.05$ and various kR . Plot (a) shows I in semi-log scale as a function of angle for the arrangement shown in Fig. 1. Plot (b) shows the same curves except as a function of qR in log-log scale. All three power-law regions of Eq. (5) can be seen in (b) along with the Guinier and ρ -crossovers discussed in Sections 4 and 5.

“ q -space” refers to the analysis of scattering quantities, like the intensity, when described as a function of q rather than θ . The q -space patterns depicted in Fig. 2 are also known to occur for particles of greater refractive index, see e.g. [1,2].

In general, the patterns are *empirically* found to be controlled by the phase shift parameter

$$\rho = 2kR \operatorname{Re}\{m - 1\}. \quad (4)$$

The physical meaning of ρ is the difference in wave phase between a ray passing through the center of the sphere along the forward direction and a ray in the incident wave traversing the same distance in vacuum [21,23]. Although only real valued m are considered in this work, in which case the $\operatorname{Re}\{\dots\}$ filter in Eq. (4) is unnecessary, the filter is nonetheless shown to remind the reader that the phase shift parameter relates only to the refractive, not absorptive, properties of the particle. In terms of ρ , the q -space power-law patterns are

$$I(\theta) \simeq \begin{cases} (qR)^0 & 0 \leq qR \leq \pi/2, \\ (qR)^{-2} & \pi/2 \leq qR \leq \rho \quad \text{if } \rho > 1, \\ (qR)^{-4} & \rho \leq qR. \end{cases} \quad (5)$$

Each of these three power-law regions can be seen in (b) of Fig. 2, where the transition from one power-law to the next is called a crossover. In general, the patterns separate into two groups. If $\rho < 1$, the $(qR)^0$ and $(qR)^{-4}$ power-laws are present. When $\rho > 1$, an approximate $(qR)^{-2}$ power-law appears along with an additional crossover, called the ρ -crossover.

Eq. (5) and several related patterns are described in detail in [1–3,5,8]. In each case, these patterns are established in an empirical manner: The Mie solution is used to generate intensity curves for a variety of particles. The curves are then collectively studied to identify commonalities between them using generalized unitless quantities like kR , qR , and ρ . Because of this empirical basis, it is not clear *why* the patterns occur or what their physical significance may be.

3. A microphysical model

In solving the frequency domain Maxwell equations for a given situation, one can in general choose between two *mathematically* equivalent approaches; the equations can be combined into a single wave equation and solved as a boundary value problem, or the solution can be formulated directly as an integral equation over the particle volume [14,18]. Although both approaches are equivalent in that they provide exactly the same solutions, they do not necessarily provide the same physical insight, see e.g. [15–18]. Here a combination will be considered. The boundary value solution for the electric field inside a spherical particle, i.e., the Mie solution, will be combined with the integral equation expression for the scattered field. This procedure is redundant since the Mie solution readily provides the scattered field. However, this combination will enable a graphically based technique, phasor analysis, which will eventually reveal the meaning of the power-law crossovers.

The observable quantity of interest in this work is the far-field scattered intensity, which can be calculated directly from the scattered electric field \mathbf{E}^{sca} . The volume integral equation (VIE) for this field is [19]

$$\mathbf{E}^{\text{sca}}(R_i \hat{\mathbf{r}}) = \frac{k^2}{4\pi} \frac{\exp(ikR_i)}{R_i} (m^2 - 1) (\hat{\mathbf{I}} - \hat{\mathbf{r}} \otimes \hat{\mathbf{r}}) \cdot \int_{V_{\text{int}}} \mathbf{E}^{\text{int}}(\mathbf{r}') \exp(-ik\hat{\mathbf{r}} \cdot \mathbf{r}') d\mathbf{r}'. \quad (6)$$

The internal field \mathbf{E}^{int} in Eq. (6) is calculated following [20]. It is shown in [16] that due to the reflection symmetry of the scattering arrangement considered here, only the x -component of \mathbf{E}^{int} contributes to \mathbf{E}^{sca} when \mathbf{r} is in the y - z plane. This simplifies Eq. (6) to

$$\mathbf{E}^{\text{sca}}(\theta) = \frac{k^2}{4\pi} \frac{\exp(ikR_i)}{R_i} (m^2 - 1) \int_{V_{\text{int}}} E_x^{\text{int}}(\mathbf{r}') \exp(-ik\hat{\mathbf{r}} \cdot \mathbf{r}') d\mathbf{r}' \hat{\mathbf{x}}, \quad (7)$$

where E_x^{int} denotes the x -component of the internal field. Note from Fig. 1 that $\hat{\mathbf{r}}$ depends only on θ . By discretizing

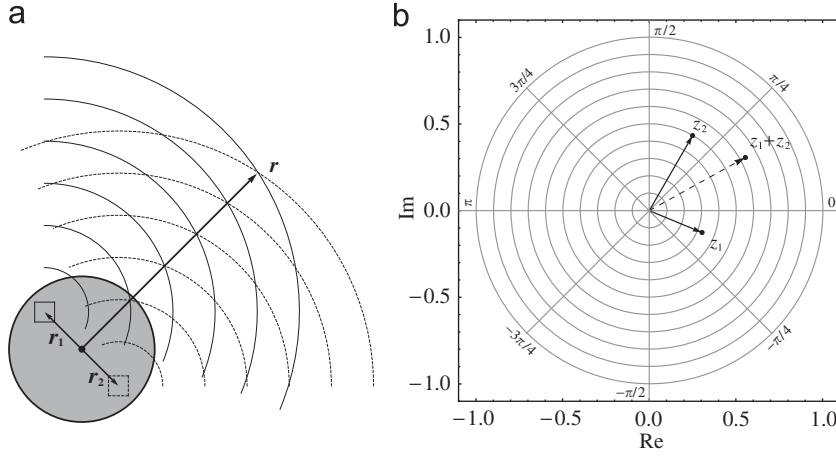


Fig. 3. A microphysical model. Sketch (a) depicts two differential volume elements, positioned at \mathbf{r}_1 and \mathbf{r}_2 , and each element's wavelet indicated by solid and dashed curves, respectively. The phasor plot (b) shows an example of phasors that could correspond to the wavelets in (a). These phasors are labeled z_1 and z_2 . A phasor is represented here as a point in the complex plane denoting the endpoint of the phasor vector given by Eq. (9). The wavelet addition in Eq. (8) giving \mathbf{E}^{sca} can be graphically represented as the vector sum of the phasors, indicated here by the dashed arrow in (b).

this integral, the scattered field can be expressed as the sum

$$\mathbf{E}^{sca}(\theta) = \frac{\exp(ikR_l)}{R_l} \lim_{\Delta V \rightarrow 0} \sum_i z_i(\theta) \hat{\mathbf{x}}, \quad (8)$$

where

$$z_i(\theta) = \frac{k^2}{4\pi} (m^2 - 1) E_x^{int}(\mathbf{r}_i) \exp(-ik\hat{\mathbf{r}} \cdot \mathbf{r}_i) \Delta V \quad (9)$$

and ΔV is a differential volume element centered at \mathbf{r}_i in the particle.

The physical picture embodied by Eq. (8) is as follows [14]: The particle can be envisioned as an array of many differential volume elements, each of which radiates a spherical wave from its location \mathbf{r}_i to the observation point \mathbf{r} in the far-field, see (a) in Fig. 3. The phase of each spherical wave is given by the scattering-angle-dependent complex-valued number, or phasor, z_i in Eq. (9). These spherical waves, or wavelets for short, superimpose at \mathbf{r} to constitute the scattered field. A unique feature of this model is that one can plot the wavelet phasors z_i as points, which are at the vector heads of the phasors, in the complex plane and then visually study how various regions within the particle contribute to the scattered field, see (b) in Fig. 3 [17]. This graphically based phasor analysis can easily be used to understand the angular structure of the scattered intensity since, in the far-field zone, the scattered wave is transverse and thus can be expressed in terms of the electric field phasors directly,

$$I(\theta) = \frac{1}{2} \sqrt{\frac{\epsilon_o}{\mu_o}} \left| \sum_i z_i(\theta) \right|^2. \quad (10)$$

Note that this phasor concept is commonly used in elementary analyses of diffraction and interference in many optics texts, see e.g. [36]. For a more detailed description of phasor analysis in the microphysical model and its applications, see [17].

4. The weak refraction regime

When $\rho < 1$, the intensity curves follow the $(qR)^0$ and $(qR)^{-4}$ power-laws with only the Guinier crossover, recall Fig. 2. One can regard $\rho < 1$ as the weak refraction regime, in which case the internal field is approximately equal to the incident field,

$$\mathbf{E}^{int}(\mathbf{r}) \simeq \mathbf{E}^{inc}(\mathbf{r}) \quad \text{if } \rho < 1. \quad (11)$$

Eq. (11) is typically called the Rayleigh–Debye–Gans (RDG) approximation [23]. Using Eqs. (1) and (11), Eq. (7) becomes

$$\mathbf{E}^{sca}(\theta) \simeq \frac{k^2}{4\pi} \frac{\exp(ikR_l)}{R_l} (m^2 - 1) E_o^{inc} \int_{V_{int}} \exp(i\mathbf{q} \cdot \mathbf{r}') d\mathbf{r}' \hat{\mathbf{x}}, \quad \rho < 1, \quad (12)$$

where Eq. (3) has been used. This is the widely known result that the far-field scattered wave for a particle in the RDG approximation is proportional to the Fourier transform of the particle volume from real space into q -space [21–25]. Use of this same approximation in Eq. (9) gives for the wavelet phasors,

$$z_i(\theta) = \frac{k^2}{4\pi} (m^2 - 1) E_o^{inc} \exp(i\mathbf{q} \cdot \mathbf{r}_i) \Delta V. \quad (13)$$

Now consider how these phasors are distributed in the complex plane. When the observation point is in the exact forward direction, $\theta = 0$ and hence $q = 0$ via Eq. (3), the exponential in Eq. (13) becomes one. This corresponds to a phasor plot with each phasor having the same magnitude and phase angle; all phasors overlap at a single point on the positive real axis. Note that if m has a nonzero imaginary part, the phasors would in general not reside on the positive real axis but would still all overlap at a single point. The scattered intensity in the forward direction follows from Eq. (10),

$$I(0) = \sqrt{\frac{\epsilon_o}{\mu_o}} \frac{k^4}{32\pi^2} (m^2 - 1)^2 (E_o^{inc})^2 (V_{int})^2, \quad (14)$$

where use has been made of the relation $\sum_i \Delta V = V_{int}$. Eq. (14) demonstrates that the forward scattered intensity in the RDG approximation is proportional to the square of the particle volume [22]. The reason that this happens is because all of the particle's wavelets are exactly in phase in the forward direction, i.e., they all constructively interfere.

Returning to Eq. (2), one can see that as θ increases from zero, the projection of \mathbf{q} onto a wavelet source's location \mathbf{r}_i can deviate from zero and cause the phase in the exponential of Eq. (13) to change. The direction of \mathbf{q} separates the particle's interior into hemispheres; one hemisphere for locations with positive projection $\mathbf{q} \cdot \mathbf{r}_i > 0$, and the other for those with negative projection $\mathbf{q} \cdot \mathbf{r}_i < 0$. The separation between the hemispheres is given by the primary plane. This plane passes through the particle's center and is perpendicular to \mathbf{q} , hence all wavelets centered on this plane have $\mathbf{q} \cdot \mathbf{r}_i = 0$. The sketch in Fig. 4 illustrates this situation with the positive and negative-projection hemispheres indicated by red and blue shading, respectively.

Now suppose that the scattering angle is fixed, as in Fig. 4, and consider wavelet source locations centered on two parallel planes displaced from the primary plane by w within each hemisphere. The \mathbf{r}_i contained in these displaced planes have equal but opposite projections along \mathbf{q} . The phase of the phasors corresponding to locations in the plane displaced along \mathbf{q} are positive since $\mathbf{q} \cdot \mathbf{r}_i > 0$, see the red plane in Fig. 4. Conversely, the phase of the phasors associated with the plane displaced along $-\mathbf{q}$ have the same magnitude but opposite sign since $\mathbf{q} \cdot \mathbf{r}_i < 0$, see the blue plane in Fig. 4. This phase-angle behavior shows that phasors belonging to the $\mathbf{q} \cdot \mathbf{r}_i > 0$

hemisphere rotate counter-clockwise about the origin in the complex plane as θ increases, whereas phasors in the $\mathbf{q} \cdot \mathbf{r}_i < 0$ hemisphere rotate clockwise. Given that all the phasors have the same magnitude in the RDG approximation, this means that the head points of the phasors collectively form an arc-shaped distribution centered on the origin in the complex plane.

Fig. 5 shows the normalized intensity curve as calculated from Mie theory for a spherical particle with $kR = 4.0$ and $m = 1.05$, hence $\rho = 0.4$. Four points on the curve, labeled $a-d$, are identified along with the phasor plots for each of these points. Note that peaks are chosen rather than valleys because the power-laws relate to the envelopes bounding an intensity curve, recall Fig. 2. Although $\rho < 1$ in this case, the exact Mie internal field is used here rather than Eq. (11) in order to validate the following conclusions predicated upon the RDG-approximation. By comparing the plots to the respective points on the curve, one can see how the phasors spread in a counter-rotating manner as qR increases. For point a , which corresponds to the forward direction, all the phasors are closely grouped around the positive real axis as mentioned above. This grouping indicates that the particle's wavelets constructively interfere in the forward direction, resulting in a maximum value for I . At point b , one can see that the phasors have spread from the real axis into an arc-like distribution with some phasors at opposition about the origin, i.e., separated by a phase of π . This phasor opposition indicates the onset of destructive interference between the corresponding wavelets, and as a consequence, the intensity is decreased compared to its value in the forward direction. The phasor plots for points c and d form a complete ring indicating further

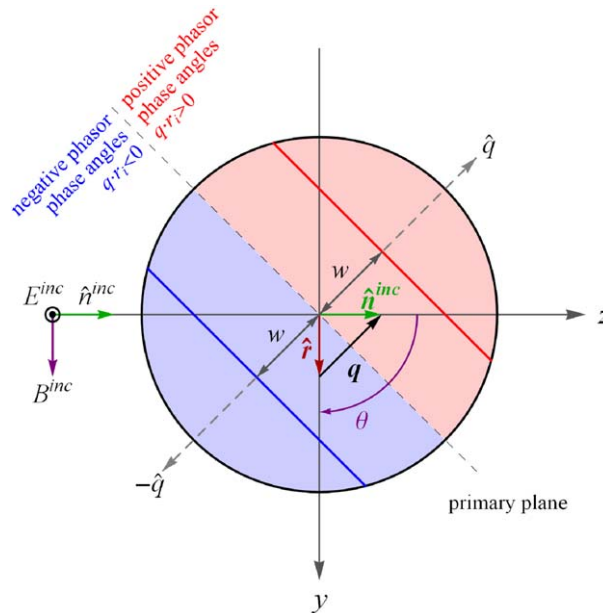


Fig. 4. Location of wavelets with positive (red) and negative (blue) phasors. The direction of the scattering wave vector \mathbf{q} is shown for a scattering angle of $\theta = \pi/2$ along with the primary plane and two parallel planes displaced from the primary plane by w . (For interpretation of the references to color in this figure legend, the reader is referred to the web version of this article.)

destructive interference, and hence further decrease of I . Note in Fig. 5 that the phasor distribution is not exactly the ring shape as predicted from the RDG approximation; it has a radial “thickness” that is due to the slight departure of the exact Mie internal field from the incident field. Also note that the clumping of phasors for points c and d is due to the finite discretization of the particle volume that is required in the numerical calculations. The task in the following will

be to show how this phasor addition can quantitatively account for the power-laws in Eq. (5) and the associated crossovers.

Recall from Fig. 4 and Eq. (13) that all phasors corresponding to volume elements centered on a plane perpendicular to \mathbf{q} share the same phase angle; the phase angle depends only on the separation of this plane from the primary plane. Given this, consider dividing the particle into slices formed by a sequence of parallel

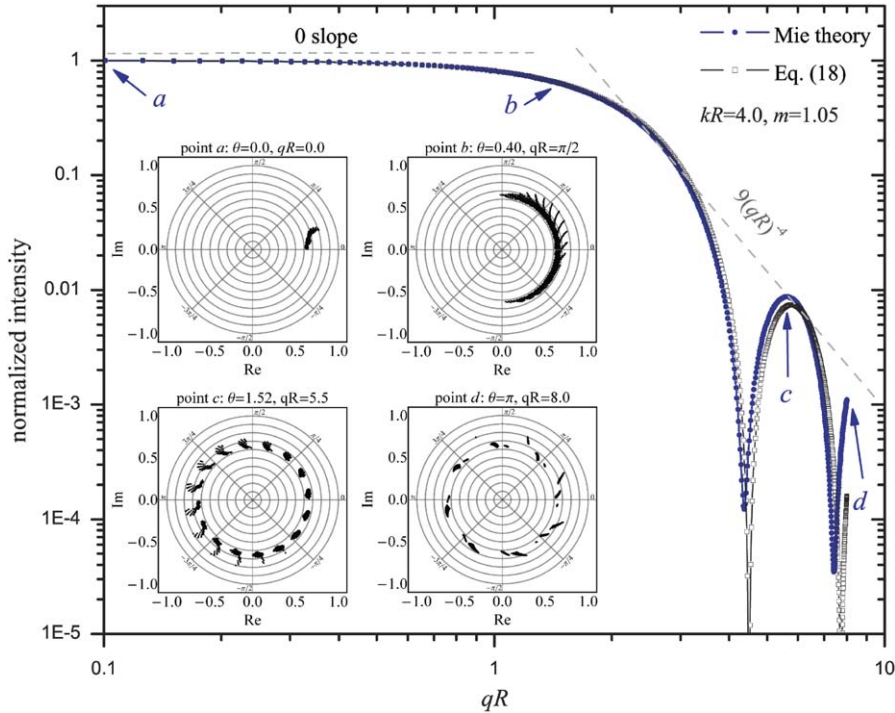


Fig. 5. Normalized intensity, blue solid curve, for a particle with $kR = 4$ and $m = 1.05$ as calculated from Mie theory. The gray broken curve shows the intensity as calculated from Eq. (18), which is equivalent to the RDG approximation of the Mie solution. The inset plots show the particle's phasor distributions for the corresponding points labeled a – d on the Mie curve. Note that the clumping of the phasors in c and d is an artifact of the discretization of the particle volume required in the numerical evaluation of Eq. (9). (For interpretation of the references to color in this figure legend, the reader is referred to the web version of this article.)

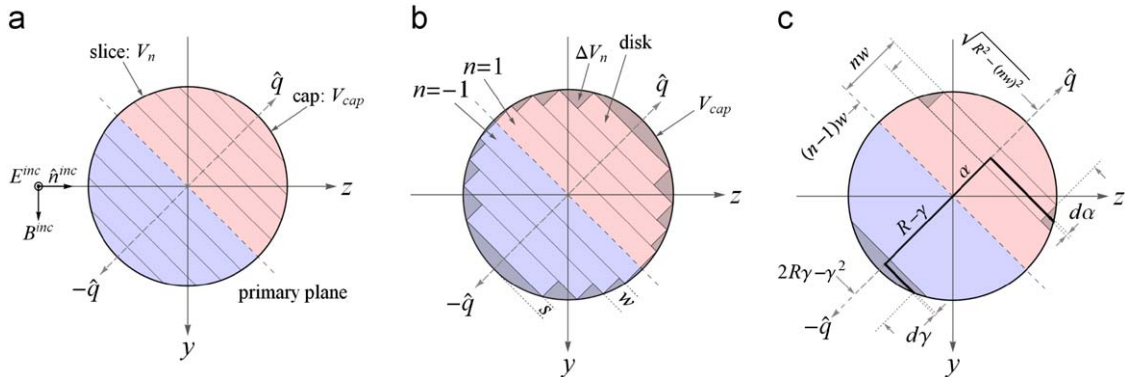


Fig. 6. Division of the particle volume used to derive the Porod law of Eq. (22). Sketch (a) shows the particle divided into slices V_n and end caps V_{cap} . Sketch (b) shows how the slices are themselves divided into disks and leftover volumes ΔV_n . Two disks, $n = 1$ and $n = -1$, are identified to show an example of a disk pair for which the associated phasors collectively cancel as described in the text. Sketch (c) shows the quantities needed to derive the integrals in Eqs. (18)–(21) leading to the Porod law equation (22).

planes separated by w as shown in Fig. 4 and (a) and (b) of Fig. 6. Let the thickness of a slice be such that the change of phase between the planes forming the slice be $\pm\pi$, where the sign depends on which hemisphere the slice is in. From the dot product in Eq. (13), this thickness is q -dependent and is given by

$$qw = \pi, \quad (15)$$

which shows that as θ increases, and thus increases q via Eq. (3), the slice thickness decreases. The slices are denoted by V_n where the nonzero integer n identifies a specific slice; positive n if the slice resides in the positive hemisphere and negative n for the negative hemisphere. The total number of slices depends on the specific values of q and R . In general, the sphere cannot be partitioned completely into slices alone. Incomplete partitioning results in two spherical cap regions, denoted V_{cap} , located at the particle's "tip" in the $\pm\mathbf{q}$ directions. The thickness of these cap volumes is s , where $s \leq w$, see (b) in Fig. 6.

In the near-forward direction, where $\theta \rightarrow 0$, Eqs. (3) and (15) show that the slice thickness w becomes infinite. Consequently, the sphere is not divisible into slices, but rather, consists only of the two cap volumes. Because $q \rightarrow 0$ as $\theta \rightarrow 0$, Eq. (13) shows that the phase of the particle's phasors is infinitesimal. Hence, one cap includes the phasors with infinitesimally positive phase angles and another includes the phasors with infinitesimally negative phase angles. At some point as θ increases, w decreases enough via Eq. (15) that the phase of phasors associated with the tips of the particle in the $\pm\mathbf{q}$ directions increase to $\sim \pm\pi/2$, respectively. These tip regions are located at $\mathbf{r}_1 = R\hat{\mathbf{q}}$ and $\mathbf{r}_2 = -R\hat{\mathbf{q}}$.

Let q_1 denote the q -value at which phasors associated with the particle's tip regions approach $\sim \pm\pi/2$ in phase. Then

$$\mathbf{q}_1 \cdot (\mathbf{r}_1 - \mathbf{r}_2) = 2q_1R = \pi, \quad (16)$$

which shows that at q_1 the wavelets near the tips of the particle begin to destructively interfere, thus diminishing the scattered intensity. Eq. (16) can be rearranged to identify the q -value at which this decrease becomes appreciable,

$$q_1R \simeq \frac{\pi}{2} \quad \text{or} \quad q_1 \simeq \frac{\pi}{2R}. \quad (17)$$

Point b in Fig. 5 illustrates the appreciable beginning of this decrease. One can see the destructively interfering tip phasors in the corresponding phasor plot at the ends of the arc-shaped distribution.

Eq. (17) identifies the first crossover between the $(qR)^0$ and $(qR)^{-4}$ power-law regions. This crossover is commonly called the Guinier crossover due to its use in X-ray scattering, where the RDG approximation usually holds well [3,22]. The Guinier crossover occurs for any particle shape; if it is nonspherical and randomly oriented, the radius of gyration takes the place of R in a formulation similar to Eq. (17) [22].

In order to explain the cause of the $(qR)^{-4}$ power-law, consider dividing each slice V_n into two parts. One part is the largest right circular cylinder (or disk for short) with thickness w that is contained entirely within the slice. The other part is the volume near the particle surface that is

also contained within the slice but outside of the disk. Call this latter volume ΔV_n . Examples of both of these are shown in (b) in Fig. 6, where the ΔV_n are shaded and the disks are not. Each disk in the positive hemisphere has a twin in the negative hemisphere, where each disk in the pair is the mirror image of the other about the primary plane. An example of such a pair is the $n = 1$ and -1 disks indicated in (b) in Fig. 6. By definition, the overall difference in phase of the phasors associated with any one of these disks is $\pm\pi$. Therefore, the phasors associated with a disk pair exactly cancel and hence make no contribution to I . However, phasors associated with the volumes ΔV_n , corresponding to a disk pair, only partially cancel. It is shown below that this is because the curvature of the particle surface upsets the complete phasor cancellation occurring for the disk pair.

The sketches in Fig. 7 illustrate how the above wavelet interference occurs in more detail; here the $n = 3$ and -3 slices of the sphere are considered, where each slice is subdivided into five thinner volumes. Sketch (a) shows the disk pair associated with the slices and labels the five thinner divisions of the two disks $a+$ through $e+$ for $n = 3$ disk, and $a-$ through $e-$ for $n = -3$. Since the difference in phase across a slice is π , the phasors associated with the wavelets contained in disk $n = 3$ are distributed between 0 and π in the complex plane. Conversely, those associated with the $n = -3$ disk are distributed between 0 and $-\pi$. The points shown in (b) figuratively represent the phasor distribution corresponding the thinner disk volumes. Because each thin disk has the same volume as the others, the magnitude of the associated thin-disk-phasors are all equal, recall Eq. (9). Consequently, the total sum of all phasors associated with the $n = 3$ and -3 disk-pair exactly cancel, as is seen by the symmetric distribution of the phasors about the origin in (b). Now consider sketch (c), which shows the same slice pair, except here the leftover volumes $\Delta V_{\pm 3}$ are now subdivided into five thinner volumes. These thinner volumes are also labeled $a+$ through $e+$, and $a-$ through $e-$, and the associated phasors are shown in (d). Because of the curvature of the sphere's surface, the volumes of the subdivisions $a+$ through $e+$, and $a-$ through $e-$, are not equal, and hence, their phasors do not share the same magnitude. This means that the phasors do not exactly cancel and hence the corresponding wavelets do contribute to the scattered intensity; this is what is meant in the above statement, "... the curvature of the particle surface upsets the complete phasor cancellation..." The end effect is that the intensity curve for $\rho < 1$ can be calculated from the phasors corresponding to the shaded region near the particle surface shown in (b) of Fig. 6.

To be more quantitative, Eq. (10) can be evaluated over this shaded volume. To do this, one must evaluate the integral in Eq. (12) over the portion of the particle consisting of ΔV_n and V_{cap} . From Eqs. (10) and (12), this gives

$$\frac{I(\theta)}{I(0)} \simeq \frac{1}{(V_{int})^2} |\Im_1(\theta) + \Im_2(\theta)|^2, \quad (18)$$

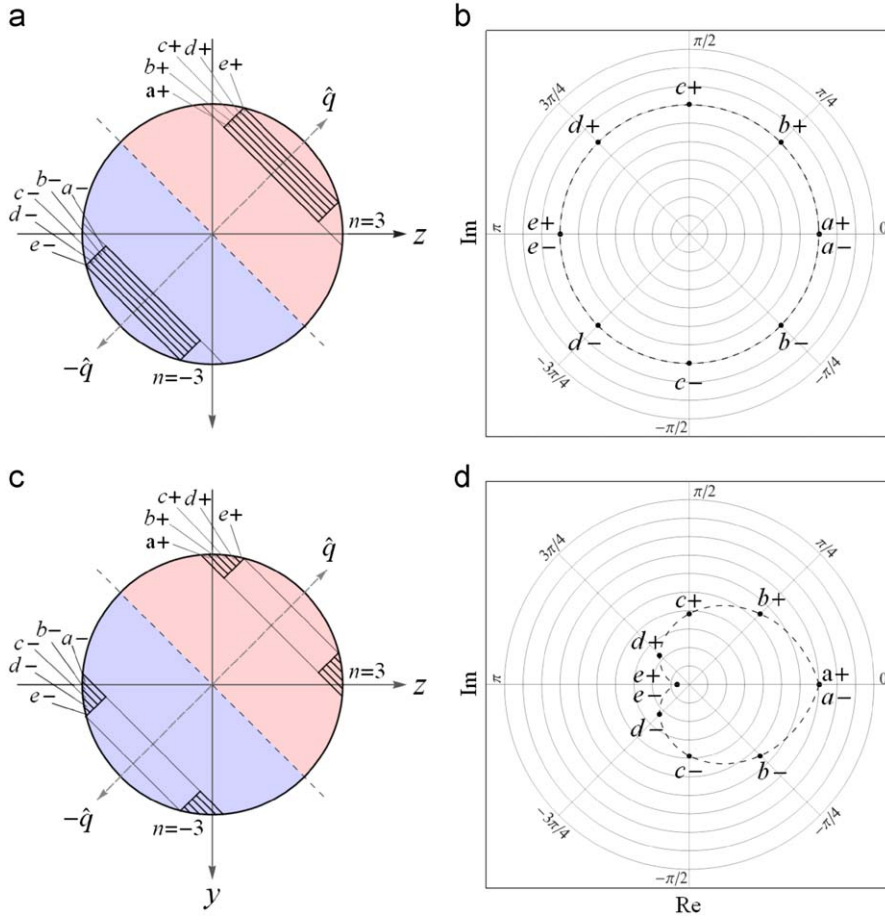


Fig. 7. Illustration how the surface of the particle causes incomplete destructive interference between the wavelets in the weak-refraction regime. Sketches (a) and (c) show the subdivision of the $n=3$ and -3 slice pair into thinner volumes labeled $a+$ through $e+$, and $a-$ through $e-$, respectively. Phasor plots (b) and (d) show the corresponding phasors. Note that no scale is given in the plots since only the qualitative distribution of the phasors is important.

where

$$\mathfrak{I}_1(\theta) = \int_{\sum \Delta V_n} \exp(i\mathbf{q} \cdot \mathbf{r}') d\mathbf{r}', \quad \mathfrak{I}_2(\theta) = \int_{\sum V_{cap}} \exp(i\mathbf{q} \cdot \mathbf{r}') d\mathbf{r}'. \quad (19)$$

The notation $\sum \Delta V_n$ represents the volume of the particle occupied by all ΔV_n and $\sum V_{cap}$ represents both cap volumes. Using the quantities defined in (c) in Fig. 6, one can eventually derive the following expressions for the integrals in Eq. (19):

$$\mathfrak{I}_1(\theta) = 2\pi \int_{(n-1)w}^{nw} (n^2 w^2 - \alpha^2) \cos(q\alpha) d\alpha, \quad (20)$$

$$\mathfrak{I}_2(\theta) = 2\pi \int_0^s (2R\gamma - \gamma^2) \cos[q(R - \gamma)] d\gamma, \quad (21)$$

where all variables in Eqs. (20) and (21), except R , implicitly depend on θ . Also note that the identity $2\cos(x) = \exp(ix) + \exp(-ix)$ is used in deriving Eqs. (20) and (21).

Fig. 5 shows the intensity curve given by Eq. (18) plotted along with the exact Mie curve. The integrals in Eqs. (20) and (21) are evaluated numerically assuming

$k=1$ and $R=4.0/k$, hence $kR=4.0$. The close agreement between the two curves demonstrates that the wavelets contained within the particle's shaded region shown in (b) of Fig. 6 are able to account for both the power law and crossover behavior of the exact (Mie) scattered intensity. The discrepancy between the two curves is due to the departure of the exact internal field from the RDG approximation of that field. Notice from Fig. 5 that the envelope bounding the normalized intensity calculated from Eq. (18) is given by

$$\frac{I(\theta)}{I(0)} \simeq \frac{9}{(V_{int})^2 (qR)^4}, \quad (22)$$

which is exactly the angular average of the RDG approximation of the scattered intensity found in [1,22]. This envelope is also shown in Fig. 5.

The $(qR)^{-4}$ dependence in Eq. (22) is an example of Porod's law. This law, often encountered in X-ray scattering contexts, relates the large q behavior of the intensity curve to the particle surface [1,22]. Porod's law and other related aspects of scattering in the RDG approximation can also be derived mathematically from an autocorrelation based approach. This approach deals with the

intensity directly, rather than first considering the scattered field, as is done here [26–28]. Indeed, this is how the Guinier crossover and the Porod law were initially described in [22, Sections 2.1.2.3–2.1.2.5].

5. The strong refraction case

Eq. (11) no longer applies when $\rho > 1$, since in that case refraction is not weak. In the context of the phasor addition scheme developed above, this means that it is no longer possible to determine how the particle's wavelets combine simply based on the change in volume of regions like ΔV_n and V_{cap} . It is also no longer clear how \mathbf{q} controls the wavelet superposition since the inapplicability of Eq. (11) means that \mathbf{q} does not appear explicitly in the VIE as it does in Eq. (12). The most damaging consequence of these complications is that it will no longer be possible to account for the specific power-law form and crossovers quantitatively as is done in Eqs. (17) and (22). The analysis in this section will therefore be primarily qualitative, but will nevertheless reveal useful insight to the physical meaning of the $\rho > 1$ behavior of the patterns.

Now that $\rho > 1$, the internal field is no longer constant in magnitude. This means that the phasors now vary in both phase and magnitude throughout V_{int} . Consequently, the distribution of phasors in the complex plane becomes more complicated as compared to the relatively simple distributions shown in Fig. 5. To preserve the heuristic utility of the phasor plots, a color-coding scheme is introduced below that connects the phasors to their corresponding locations inside of the particle.

To describe this color coding scheme in more detail, consider Fig. 8. Plot (a) shows the scattering plane cross section through a particle with $kR = 12$, $m = 1.5$, and $\rho = 12$. The incident wave travels from left to right, recall Fig. 1. The plot shows a color-coded representation of the integrand of the VIE, Eq. (7), when the observation point is in the forward direction $\theta = 0$, i.e., $\hat{\mathbf{r}} = \hat{\mathbf{n}}^{inc}$. The color and brightness of each point in plot (a) represents the phase

and magnitude of the integrand, respectively. Plot (b) shows the phasor distribution for this same particle as calculated from Eq. (9) using the exact Mie internal field. Here, the same color coding scheme is used as in (a). All regions in plot (a) with the same color correspond to phasors in (b) with the same phase angle. Regions with the same brightness in (a) correspond to phasors with the same magnitude in (b). This color coding allows the two plots to be compared directly. For example, three regions inside the particle are identified in (a) by white ellipses. The brightness of the color in these regions is greatest indicating that the internal field magnitude is greatest there. These regions are typically called “hot spots” and arise as a consequence of refraction and the particle shape, e.g. see [29–31, 33–35]. The phasors associated with these hot spots are circled in (b). One can see that these phasors have the largest magnitude and have the same green color as the corresponding regions in (a). Note that the phasor distribution is normalized for clarity here and in the following.

The phasors in (b) in Fig. 8 are qualitatively clustered into groups within which the phasors have similar magnitude and phase. An exact quantitative condition for the maximum variation in phase or magnitude defining a group is not crucial here; the group concept is only intended to enable a qualitative analysis of the distribution's evolution. As θ increases from zero, each phasor will change in phase and hence will rotate around the origin in the complex plane as the exponential in Eq. (9) changes. However, the colors of the phasors *are not changed* from their $\theta = 0$ value as they undergo this rotation. This means that one can track the evolution of each phasor as θ changes simply by following its color over a sequence of phasor plots.

Fig. 9 shows the normalized scattered intensity curve for the same sphere as in Fig. 8. This curve displays all three power-law regions of Eq. (5), separated by the Guinier and ρ - crossovers. Note that there is a sharp backscattering peak, the glory, that is not described by the patterns and hence is ignored in the following. Six points

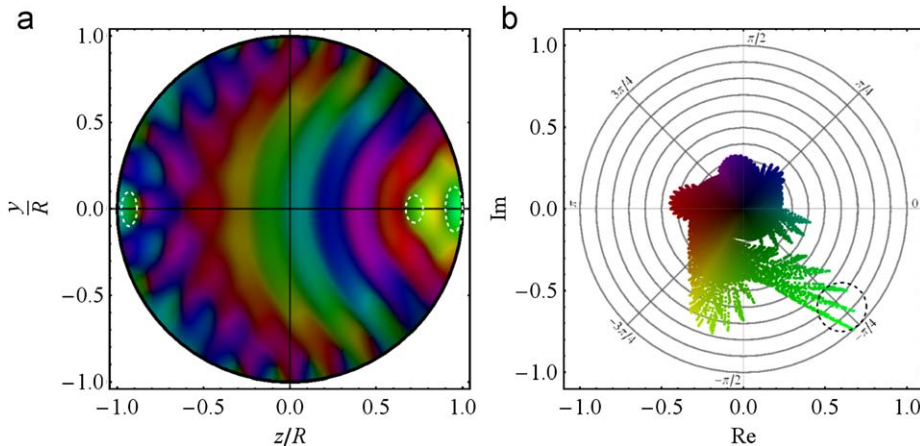


Fig. 8. Color-coded connection between the interior of a spherical particle (a) and the corresponding phasor distribution (b). The particle's size parameter, refractive index, and phase shift parameter is $kR = 12$, $m = 1.5$, and $\rho = 12$, respectively. See text for further explanation. (For interpretation of the references to color in this figure legend, the reader is referred to the web version of this article.)

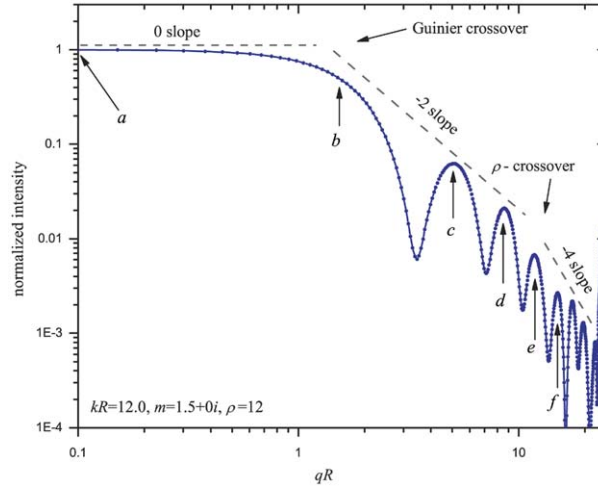


Fig. 9. Normalized scattered intensity curve for the particle in Fig. 8. The points labeled *a–f* correspond to the phasor plots in Fig. 10 labeled likewise.

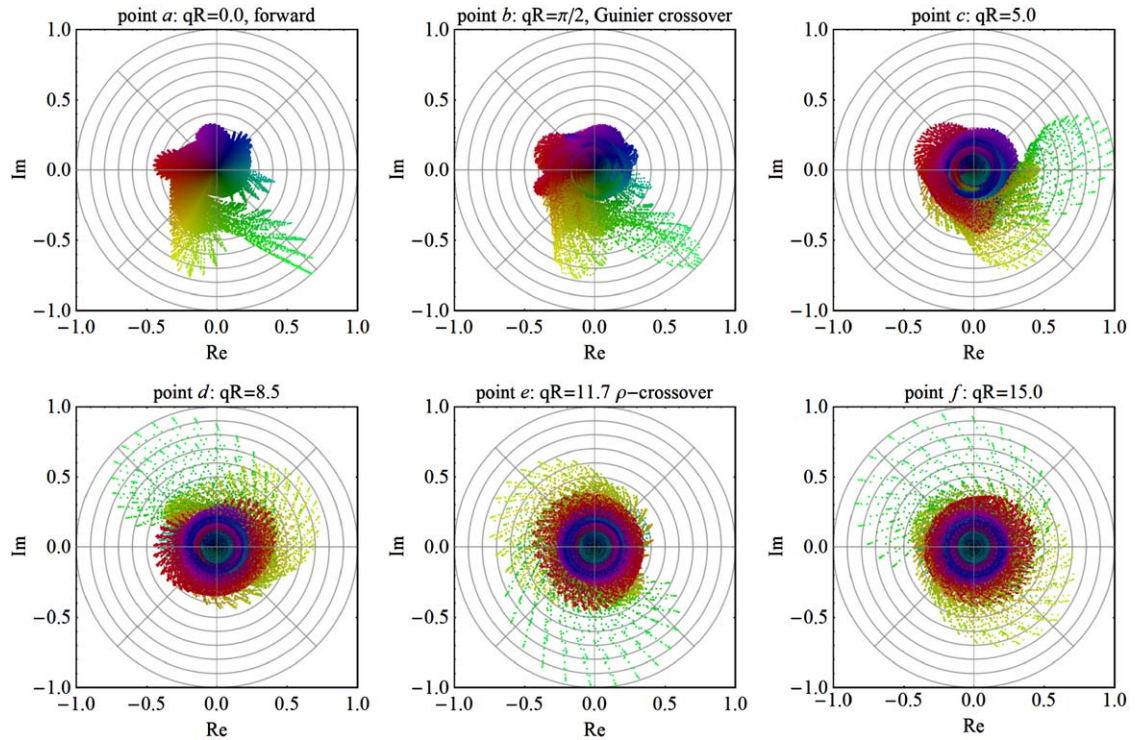


Fig. 10. Color-coded phasor distributions for the points indicated on the scattering curve in Fig. 9. Distribution *a* is exactly the same as (b) in Fig. 8. The phasor colors are assigned according to the distribution at $\theta = 0$, plot *a*. See text for further discussion. (For interpretation of the references to color in this figure legend, the reader is referred to the web version of this article.)

on the curve are labeled *a–f* and the phasor distributions for each of these points is displayed in Fig. 10. The phasor plot *a*, which corresponds to the forward direction $\theta = 0$, is exactly the same as (b) in Fig. 8.

Now compare plots *a* and *b* in Fig. 10. Between these plots, the scattering angle advances from zero to the Guinier crossover, and as a consequence, the phasors spread in phase angle resulting in the slightly twisted

appearance of *b*. Remember that the colors are assigned to the phasors when $\theta = 0$ and these colors are not changed as the phasors rotate to other positions in the complex plane. Recall from Section 4 that spreading of the phasors corresponds to the onset of destructive interference between the particle's wavelets, and hence, a reduction of the scattered intensity. Because the phasors in plot *a*, which are identical to (b) in Fig. 8, are spread around the

origin, there is a large degree of cancelation among them. This is contrary to the $\rho < 1$ case where all phasors are clustered together when $\theta = 0$.

The cancelation of phasors in plot *a* occurs between different phasor groups, i.e., between different colors. This will be called *inter-group* cancelation. As the scattering angle θ increases from zero to the Guinier crossover, plot *b* in Fig. 10, the phasors spread, further enhancing inter-group cancelation and thus leading to a decrease in the scattered intensity. The magnitude of this *enhancement* in inter-group cancelation becomes significant only when the scattering angle is large enough to sufficiently advance the phase of the exponential in Eq. (9) relative to kR . This shows that the Guinier crossover occurs in the $\rho > 1$ case for the same reason that it does in the $\rho < 1$ case; *wavelets located near the “tips” of the particle in the $\pm \mathbf{q}$ direction begin to interfere destructively, thus reducing the scattered intensity.*

Comparison of the structure of plots *b–d* shows that the phasors continue to spread in phase angle as θ increases. Very careful inspection of these distributions reveals that by the time the ρ -crossover is reached at point *e*, the phasors within a given group have spread by an amount of nearly π in phase. This can be seen by the smearing of a given color over an angular range of π in plot *e*. Once the phasors of a given group spread to this extent, they begin to cancel each other, and hence constitute *intra-group* cancelation. Notice though, that inter-group cancelation still occurs.

Before the ρ -crossover, the contributions to the scattered intensity come from phasors of different groups that partially cancel each other. To describe this in more detail, return to plot *a* in Fig. 10 and find the phasor group, colored green, that consists of the largest magnitude phasors. This group is poorly canceled by other groups, or colors, due to its greater than average magnitude, see plots *a–d*. It is only after the ρ -crossover is reached, and intra-group cancelation begins, that the contribution to the scattered intensity from this group is most reduced. One can now return to plot (a) in Fig. 8 and see that this (green) group belongs to the region in the sphere where the internal field magnitude is greatest, denoted by the brightest-green circled regions. These are the particle's so-called “hot spots.” The cause of hot spots is related to an interplay between refraction and the particle shape. One can understand the involvement of refraction by realizing that there are no hot spots for the $\rho < 1$ case where refraction is weak. The involvement of the particle surface can be understood by realizing that a highly refractive plate of glass under plane wave illumination at normal incidence shows no hot spots because of the absence of a convex surface to “focus” the wave. The implication then, is that *the cause of the decrease in the scattered intensity at the ρ -crossover is due to destructive interference between wavelets within the particle's hot spots.* This also shows why the decrease depends specifically on ρ , since it is ρ that describes the overall degree of refraction in the particle. Further evidence for this explanation is given in the following section.

As a side note, recall that a major difference between the phasor distribution at $\theta = 0$ in the $\rho < 1$ and $\rho > 1$

regimes is that the former is clustered tightly around the real axis while the latter is spread around the origin, cf. Figs. 5 and 10. This spread shows that a substantial degree of cancelation occurs even in the forward direction when $\rho > 1$. In contrast, the scattering angle must advance past the Guinier crossover before substantial cancelation begins in the $\rho < 1$ case. This means that a spherical particle with $\rho > 1$ has less scattered intensity in the forward direction as compared to the *same sized* particle treated in the RDG approximation. The above analysis demonstrates that the cause of this is refraction. In the forward direction the phase of the phasors is determined by the field-exponential product in Eq. (9). This exponential has the same functional form as the incident wave, Eq. (1). Then, the phase of the field-exponential product represents the difference in phase between the internal and incident waves. If ρ is large, refraction is strong, and this relative phase varies extensively throughout the particle interior. Consequently, the phasors are spread as seen in (a) in Fig. 8 thus explaining the RDG-relative reduction in forward scattered intensity described empirically in [2].

6. Appearance of length scales

From Eq. (2) one can see that \mathbf{q} has the units of inverse length. This leads to the proposition that particular features in I identifying single points in q -space represent “length scales” of the scattering system. For example, the crossovers identify such points,

$$\text{Guinier crossover : } qR \simeq \frac{\pi}{2} \rightarrow \frac{1}{q} \simeq \frac{2R}{\pi}, \quad (23)$$

$$\rho\text{-crossover : } qR \simeq \rho \rightarrow \frac{1}{q} \simeq \frac{R}{\rho}. \quad (24)$$

These length scales are described in [1]. In that work the Guinier-crossover length scale is explained by dividing the particle into “ q -regions” roughly q^{-1} in size. A scaling argument based on [32] is then used to show that the q -regions can both predict the crossover and yield Porod's law. The analysis in Section 4 above compliments this scaling argument. These considerations reveal the essential meaning of the Guinier crossover; it is the angle at which destructive interference over the maximal extents of the particle along the direction of \mathbf{q} begins to appreciably reduce the scattered intensity. In other words, this crossover “senses” R .

The essential conclusion from Section 5 is that the onset of destructive interference between wavelets within a particle's hot spots causes an enhancement in the decay of the scattered intensity with increasing angle. This interference does not occur until the angle advances sufficiently past the Guinier crossover such that $qR > \rho$. Therefore, it appears that the appropriate length scale to associate with the ρ -crossover is the average size of a particle's hot spots. To test this, Fig. 11 presents a survey of the x -component of the internal electric field inside three spherical particles in the y – z plane, recall Fig. 1. The height of the surfaces in the plots denotes the magnitude of the field component and the color denotes the phase of

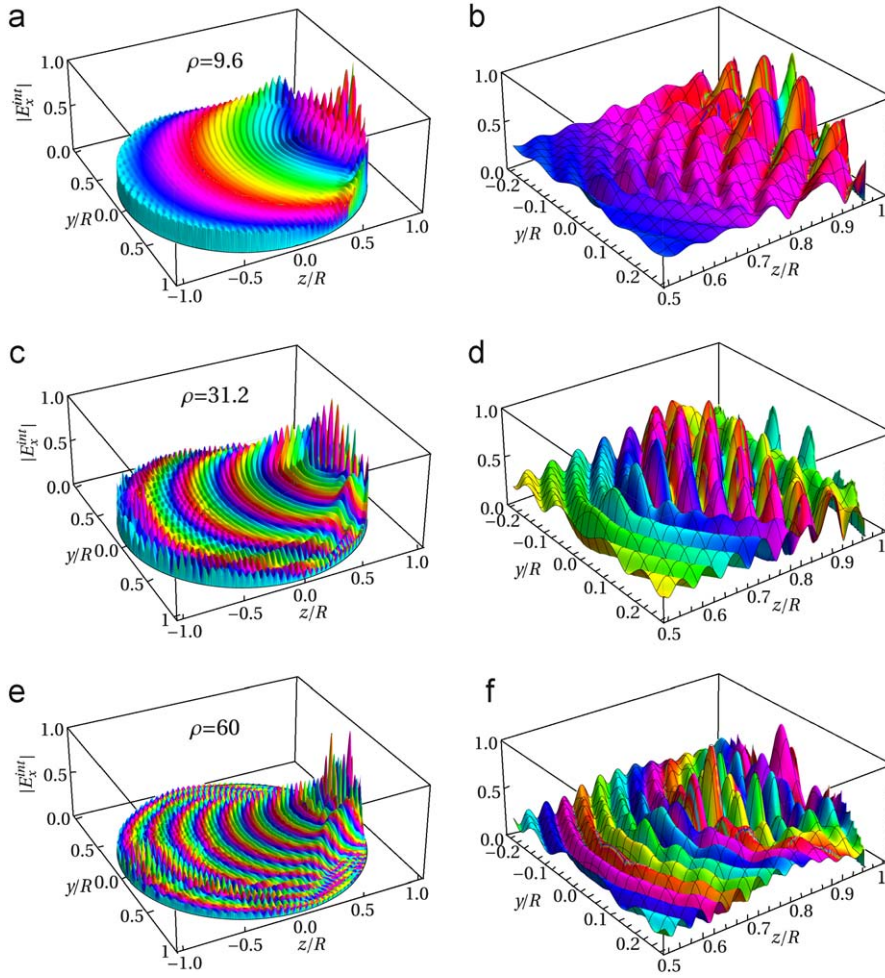


Fig. 11. Internal field magnitude and wavelet phase for three spherical particles. The height of the surfaces denotes the normalized magnitude of the x -component of the internal electric field and the colors denote the wavelet phase. The same color assignments are used as in Figs. (8) and (10). The three particles share the same size parameter $kR = 60$ but varying refractive index: $m = 1.08$ for (a), $m = 1.26$ for (c), and $m = 1.50$ for (e). Plots (b), (d), and (f) are close-up views of the hot spots of (a), (c), and (e), respectively. (For interpretation of the references to color in this figure legend, the reader is referred to the web version of this article.)

the phasors associated with the corresponding wavelets for $\theta = 0$. The same color assignment for phase angle is used here as in Figs. 8 and 10. The three particles considered in Fig. 11 share the same size parameter $kR = 60$, but differ in refractive index: $m = 1.08$ for (a), $m = 1.26$ for (c), and $m = 1.50$ for (e). Plots (b), (d), and (f) show close-up views of the hot spot regions in (a), (c), and (e), respectively. Between these three particles, the value of ρ varies from $\rho = 9.6$ in (a), to $\rho = 31.2$ in (c), and $\rho = 60$ in (e).

If it is true that the average size of the hot spots is the correct length scale to associate with the ρ -crossover, then there should be a distinct decrease in the average hot spot size as ρ increases. More specifically, this decrease should be inversely proportional to ρ given Eq. (24). Careful comparison of the plots in Fig. 11, especially the close-up views, shows that this inverse correlation between hot spot size and ρ does indeed occur. Note that a mesh is drawn on the surfaces in the close-up views to aid the eye in estimating the hot spot sizes. Further

evidence is seen in the phase. Section 5 shows that the wavelet phase when $\theta = 0$ is approximately constant over the extent of a hot spot, recall the “green” phasors of Fig. 8. The close-up views in Fig. 11 reveal this same phase behavior, which one can see from each peak in the plots being approximately the same color.

7. Discussion

There are several important practical implications of the length scales, Eqs. (23) and (24). An investigator studying a single uniform spherical particle, or a sufficiently dilute system consisting of many nearly identical spherical particles, can obtain an estimate of R directly from the measured intensity curve. The quality of this estimate would rely on the quality of the fit of the scattering curve to the $(qR)^0$, and $(qR)^{-2}$, or $(qR)^{-4}$ power-laws defining the Guinier crossover. This size estimate is largely independent of the refractive index, which one can see by the absence of m in Eq. (23). Note, however, that

there is a small m -dependence, which is described in [3]. If the scattering curve displays the ρ -crossover, then one also has an estimate for the real part of the refractive index. This results from the combination of the Guinier-crossover R -estimate with Eqs. (4) and (24). Lastly, a striking implication of the exclusive ρ dependence of the patterns is that particles with vastly different kR and $\text{Re}\{m\}$ will have intensity curves that share the same overall angular structure and crossovers provided that they also share the same value for ρ . This is called ρ -universality in [1].

8. Conclusion

This work applies a microphysical model to explain previous empirically discovered patterns in Mie theory. The model is based on the Maxwell volume integral equation and represents the particle as a collection of wavelet sources. The addition of these wavelets, which yields the far-field scattered intensity, is studied using the visually based technique of phasor analysis. A simple color coding scheme connects the phasors to their corresponding wavelets within the particle interior, and this connection reveals the cause of the patterns. In particular, the significance of crossover points between the power-laws are shown to be a consequence of destructive interference between special regions within the particle relating to the particle size and refractive index.

Acknowledgement

This work was partly supported by the National Research Council postdoctoral associateship program funded by the United States Defense Threat Reduction Agency, Contract no. DAAD17-03-C-0070.

References

- [1] Sorensen CM, Fishbach JD. Patterns in Mie scattering. *Opt Commun* 2000;173:145–53.
- [2] Berg MJ, Sorensen CM, Chakrabarti A. Patterns in Mie scattering: evolution when normalized by the Rayleigh cross section. *Appl Opt* 2005;44(34):7487–93.
- [3] Sorensen CM, Shi D. Guinier analysis for homogeneous dielectric spheres of arbitrary size. *Opt Commun* 2000;178:31–6.
- [4] Sorensen CM, Shi D. Patterns in the ripple structure of Mie scattering. *J Opt Soc Am A* 2002;19(1):122–5.
- [5] Jonsson JC, Smith GB, Niklasson GA. Experimental and Monte Carlo analysis of isotropic multiple Mie scattering. *Opt Commun* 2004;240:9–17.
- [6] Jonsson JC, Karlsson L, Nostell P, Niklasson GA, Smith GB. Angle-dependent light scattering in materials with controlled solar properties. *Solar Energy Materials and Solar Cells* 2004;84(1–4):427–39.
- [7] Jonsson JC, Smith GB, Deller C, Roos A. Directional and angle-dependent optical scattering of high-performance translucent polymer sheets for energy-efficient lighting and skylights. *Appl Opt* 2005;44(14):2745–53.
- [8] Xu M, Alfano RR. More patterns in Mie scattering. *Opt Commun* 2003;226:1–5.
- [9] Shu J, Wilson KR, Ahmed M, Leone S, Graf C, Rühl E. Elastic light scattering from nanoparticles by monochromatic vacuum-ultraviolet radiation. *J Chem Phys* 2006;124:034707-1-9.
- [10] Hubbard JA, Eckels SJ, Sorensen CM. Q-space analysis applied to polydisperse, dense random aggregates. Part Part Syst Charact 2008;25:68–73.
- [11] Weinert DW, Cleary TG, Mulholland GW, Beever PF. Light scattering characteristics and size distribution of smoke and nuisance aerosols. In: Evans DD, editor. Proceedings of the 7th International Symposium on Fire Safety Science. Gaithersburg, MD, USA: International Association for Fire Safety Science; 2003. p. 209–20.
- [12] Ferri F. Use of a charged coupled device camera for low-angle elastic light scattering. *Rev Sci Instrum* 1997;68(6):2265–74.
- [13] Mishchenko MI. Far-field approximation in electromagnetic scattering. *JQSRT* 2006;100(1–3):268–76.
- [14] Mishchenko MI, Travis LD, Lacis AA. Scattering, absorption, and emission of light by small particles. Cambridge: Cambridge University Press; 2002 freely available in the PDF format at <<http://www.giss.nasa.gov/~crimim/books.html>>.
- [15] Tyynelä J, Zubko E, Videen G, Muinonen K. Interrelating angular scattering characteristics to internal electric fields for wavelength-scale spherical particles. *JQSRT* 2007;106:520–34.
- [16] Berg MJ, Sorensen CM, Chakrabarti A. Reflection symmetry of a sphere's internal field and its consequences on scattering: a microphysical approach. *J Opt Soc Am A* 2008;25(1):98–107.
- [17] Berg MJ. A microphysical model of scattering, absorption, and extinction in electromagnetic theory. PhD dissertation, Kansas State University, Department of Physics; 2008 (freely available in the PDF format at <<http://hdl.handle.net/2097/1040>>).
- [18] Born M, Wolf E. Principles of optics, 7th ed.. Cambridge: Cambridge University Press; 1999 p. 104.
- [19] Mishchenko MI, Travis LD, Lacis AA. Multiple scattering of light by particles: radiative transfer and coherent backscattering. Cambridge: Cambridge University Press; 2006.
- [20] Bohren CF, Huffman DR. Absorption and scattering of light by small particles. New York: Wiley; 1983.
- [21] van de Hulst HC. Light scattering by small particles. New York: Dover; 1981.
- [22] Guinier A, Fournet G. Small-angle scattering of X-rays. New York: Wiley; 1955.
- [23] Kerker M. The scattering of light and other electromagnetic radiation. New York: Academic Press; 1969.
- [24] Goodman JW. Introduction to fourier optics, 3rd ed.. Greenwood Village, Colorado: Roberts & Company Publishers; 2005.
- [25] Bracewell RN. The Fourier transform and its applications. New York: McGraw-Hill; 1965.
- [26] Ciccariello S, Goodisman J, Brumberger H. On the Porod law. *J Appl Cryst* 1988;21:117–28.
- [27] Svergun DI, Koch MHJ. Small-angle scattering studies of biological macromolecules in solution. *Rep Prog Phys* 2003;66:1735–82.
- [28] Wu H, Schmidt PW. The relation between the particle shape and the outer part of the small-angle X-ray scattering curve. *J Appl Cryst* 1974;7:131–46.
- [29] Barber PW, Hill CS. Light scattering by particles: computational methods. New Jersey: World Scientific; 1990 (Section 4.5.3).
- [30] Benincasa DS, Barber PW, Zhang J-Z, Hsieh W-F, Chang RK. Spatial distribution of the internal and near-field intensities of large cylindrical and spherical scatterers. *Appl Opt* 1987;26(7):1348–1356.
- [31] Li C, Kattawar GW, Zhai P-W. Electric and magnetic energy density distributions inside and outside particles illuminated by a plane electromagnetic wave. *Opt Exp* 2005;13(12):4554–9.
- [32] Oh C, Sorensen CM. Scaling approach for the structure factor of a generalized system of scatterers. *J Nanopart Res* 1999;1:369–377.
- [33] Barton JP, Alexander DR, Schaub SA. Internal fields of a spherical particle illuminated by a tightly focused laser beam: focal point positioning effects at resonance. *J Appl Phys* 1989;65(8):2900–2906.
- [34] Chowdhury DQ, Hill SC, Barber PW. Time dependence of internal intensity of a dielectric sphere on and near resonance. *J Opt Soc Am A* 1992;9(8):1364–73.
- [35] Chowdhury DQ, Barber PW, Hill SC. Energy-density distribution inside large nonabsorbing spheres by using Mie theory and geometrical optics. *Appl Opt* 1992;31(18):3518–23.
- [36] Hecht E. Optics. San Francisco: Addison Wesley; 2002.